

Dominant 1/3-filling correlated insulator states and orbital geometric frustration in twisted bilayer graphene

Received: 31 July 2023

Accepted: 15 May 2024

Published online: 1 July 2024

 Check for updates

Haidong Tian^{1,7}, Emilio Codecido^{1,7}, Dan Mao^{2,7}, Kevin Zhang², Shi Che¹, Kenji Watanabe³, Takashi Taniguchi⁴, Dmitry Smirnov⁵, Eun-Ah Kim^{2,6}✉, Marc Bockrath¹✉ & Chun Ning Lau¹✉

Geometric frustration occurs in a lattice system when not all the interactions can be satisfied simultaneously. The simplest example is antiferromagnetically coupled spins on a triangular lattice. Frustrated systems are characterized by having many nearly degenerate ground states, leading to non-trivial phases, such as spin ice and spin liquids. To date, most studies have looked at geometric frustration of spins whereas orbital geometric frustration has been much less explored. For electrons in twisted bilayer graphene, when the electronic bands are filled to a fraction with denominator 3, Coulomb interactions and the Wannier orbital shapes are predicted to strongly constrain spatial charge ordering, leading to geometrically frustrated ground states that produce a new class of correlated insulating states. Here we report the observation of dominant, denominator 3, fractional-filling, insulating states in large-angle twisted bilayer graphene. These states persist in magnetic fields and display magnetic ordering signatures and tripled unit cell reconstruction. These results are in agreement with a strong-coupling theory for symmetry-breaking in geometrically frustrated fractional states.

Correlated insulating states observed in twisted bilayer graphene (tBLG) and moiré transition metal dichalcogenides have been intensively studied experimentally and theoretically^{1–10}. These states result from an interplay between the periodic superlattice, the magnetic field and various interactions. They can be classified into different classes of insulators with the equation

$$(n/n_0) = tb + \bar{n}, \quad (1)$$

where n is the charge density, n_0 is the density corresponding to one charge per unit cell, $b = BAe/h$ is the number of flux quanta per unit cell,

A is the area of the superlattice unit cell, B is the magnetic field, h is Planck's constant, and t and \bar{n} are constants. Here t is the Chern number, which determines the transverse conductivity $\sigma_{xy} = te^2/h$ (ref. 11). The additional quantum number \bar{n} can be viewed as the number of bound charges per unit cell¹². Both \bar{n} and t can take on either integer or fractional values and indicate the presence of physically distinct ground states^{13,14}.

To date, the vast majority of insulating states in tBLG have been observed at integer t and \bar{n} , which corresponds to integer quantum Hall or Cherninsulator states. States with fractional \bar{n} values have been observed in moiré transition metal dichalcogenides^{4–6} and are

¹Department of Physics, The Ohio State University, Columbus, OH, USA. ²Laboratory of Atomic and Solid State Physics, Cornell University, Ithaca, NY, USA. ³Research Center for Electronic and Optical Materials, National Institute for Materials Science, Tsukuba, Japan. ⁴Research Center for Materials Nanoarchitectonics, National Institute for Materials Science, Tsukuba, Japan. ⁵National High Magnetic Field Laboratory, Tallahassee, FL, USA.

⁶Department of Physics, Ewha Womans University, Seoul, South Korea. ⁷These authors contributed equally: Haidong Tian, Emilio Codecido, Dan Mao.

✉e-mail: ek436@cornell.edu; bockrath.31@osu.edu; lau.232@osu.edu

attributed to generalized Wigner crystal states in which electrons are localized in a fraction of the moiré unit cells. Very recently, signatures of states with fractional \bar{n} values have been observed in magic-angle tBLG (MA-tBLG) at twist angle $\theta = 1.06^\circ$ (ref. 15), in twisted double-bilayer graphene^{16,17} and in twisted trilayer graphene¹⁸. However, these states are much weaker than those at integer \bar{n} . These states are attributed to band-structure-driven effects that originate in momentum-space^{15,18}, although fine-tuning is required. More generally, for systems at or close to the magic angle, the close competition between the charge-ordered, symmetry-broken and fractional Chern insulators in the systems challenges the sharp theoretical understanding of the charge-ordered insulating states.

To date, very little consideration has been given to the effect of geometric frustration of charge carriers in twisted graphene systems with triangular moiré lattices. Here we report the observation of robust Chern-zero fractional correlated insulating states at a number of 1/3 fillings in tBLG with larger-than-magic twist angles ($\theta = 1.32\text{--}1.59^\circ$). These states strongly dominate over those at integer fillings and persist in perpendicular and parallel magnetic fields. They are accounted for by an orbital geometric frustration model, which is based on the three-leaved shape of the Wannier orbitals (WOs), and by considering Coulomb interactions, the site occupancy, valley polarization and exchange interactions between the charge-ordered lattice sites. In a device with a relatively small angle (but still larger than the magic angle), we observe behaviour consistent with a predicted brick-wall charge-ordered state at 1/3-fractional fillings^{8,19}. Upon applying a parallel magnetic field B_{\parallel} , we find that the $\bar{n} = \pm 8/3$ states exhibit ferromagnetic ordering, whereas the $\bar{n} = \pm 4/3$ states exhibit antiferromagnetic ordering, with a transition to a spin-aligned state observable at finite field. Moreover, in a device with a larger twist angle and expected stronger second nearest neighbour interactions, we observe a tripled unit cell, consistent with a predicted armchair phase^{8,19}. These 1/3-fractional states, therefore, originate from the WO shape and resulting geometric frustration produced by Coulomb interactions, with the phase tunable by doping and twist angle. This shows that a substantial class of phenomena in tBLG can be understood using a real-space model.

Figure 1 presents data from device D1 with $\theta = 1.32^\circ$. Figure 1a plots its two-terminal conductance G versus back gate voltage V_g (bottom axis) and \bar{n} (top axis). At $T = 0.4$ K (blue curve), conductance valleys are observed at the global charge neutrality point (CNP) of the moiré miniband. At half filling $\bar{n} = 2$, a small conductance dip is observed at $\bar{n} = +2$ and a kink at $\bar{n} = -2$. These observations are like those observed in MA-tBLG. In contrast to MA-tBLG, however, the device exhibits many fractional-filling features: deep conductance valleys are also observed at $\bar{n} = \pm 8/3$ and $\pm 4/3$ and shallower dips or shoulders emerge at $\bar{n} = \pm 2/3$ and $10/3$. Remarkably, in this device, which has θ larger than the magic angle, these 1/3-filling features are much stronger than the integer-filling features. Moreover, their conductivity, $0.1\text{--}10\ \mu\text{S}$, is much smaller than the conductance quantum $e^2/h \approx 39\ \mu\text{S}$, thus underscoring their insulating nature.

To further investigate these fractional-filling features in more detail, we measure their T dependence. Figure 1a shows that the conductance valleys rise and broaden with T until they merge into a broad background that increases at high temperatures. An Arrhenius plot of G in the conductance valleys at $\bar{n} = \pm 8/3$ shows that they can be fitted to a double exponential function. A large gap $\Delta_1 \approx 21.0$ (16.5) meV and a small one $\Delta_2 \approx 2.6$ (1.4) meV are extracted for the $\bar{n} = +8/3$ ($\bar{n} = -8/3$) state (Fig. 1b). We attribute the larger gap, which is responsible for the high-temperature behaviour, to that of the insulating state at $\bar{n} = \pm 8/3$. The smaller gap, on the other hand, probably arises from competing mechanisms at low temperatures from, for example, variable range hopping through localized states. On the other hand, the $\bar{n} = \pm 4/3$ valleys behave qualitatively differently. As T cools below 70 K (Fig. 1c), the conductance first slowly

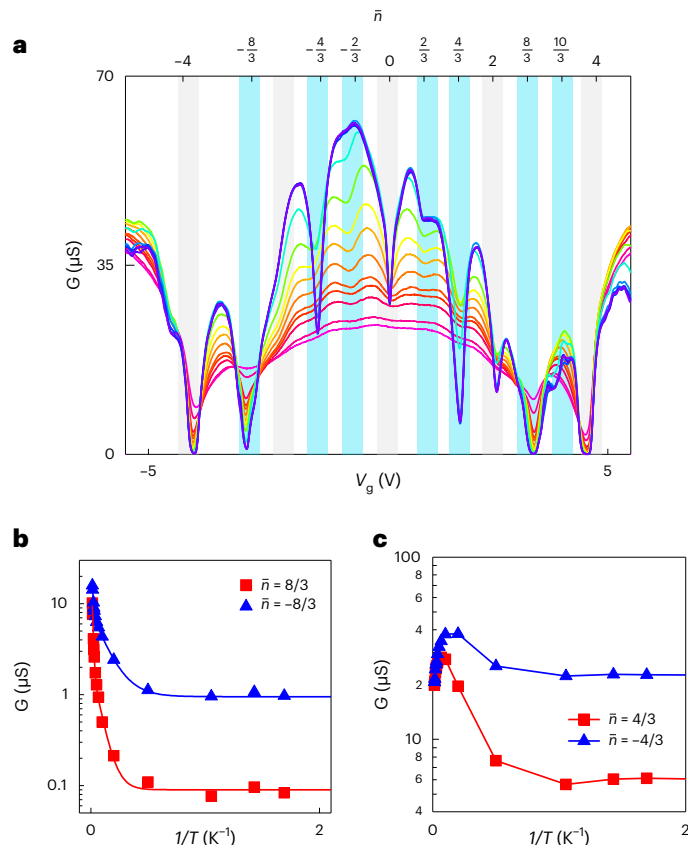


Fig. 1 | Temperature-dependent data from device D1 with $\theta = 1.32^\circ$.

a, Two-terminal G versus V_g (bottom axis) and \bar{n} at $T = 0.4, 0.6, 0.7, 0.95, 2, 5, 10, 15, 20, 25.6, 33.5, 37.6, 45, 62.6$ and 72.3 K (blue to purple, respectively). The grey and cyan vertical bands outline the features at integer and fractional fillings of the moiré superlattice, respectively. **b**, Arrhenius plot for the conductance valley at $\bar{n} = \pm 8/3$. The lines are fits to a double exponential function. **c**, Arrhenius plot at $\bar{n} = \pm 4/3$ (adjacent data points are connected by straight lines).

increases but begins to drop sharply when the temperature reaches below $T \approx 10$ K. Fitting the low-temperature regime to a thermal activation model reveals a small gap of approximately 10 K, which also agrees with the onset temperature of the conductance's nonmonotonic dependence. Thus, the $\bar{n} = \pm 4/3$ states also appear to host a substantially smaller gap of approximately 1 meV, at which the conductance appears activated, with saturation due to variable range-hopping conduction at the lowest temperature.

To understand the emergence of these fractional gapped states, we start from ref. 8, which predicts a Chern-zero insulating state in MA-tBLG at 1/3-fractional fillings^{20–22}. Unlike the momentum-space picture adopted in refs. 15,18, this strong-coupling real-space picture does not readily capture the band-structure-sensitive Chern-insulator physics. Rather, the key insight lies with the three-leaved geometry of the WOs^{20–22}, which quite generally leads to the robust presence of incompressible states at 1/3-fractional fillings and emergent geometric frustration^{20–22}. We generalize the model of ref. 8 to $\bar{n} = \pm 8/3$ and $\bar{n} = \pm 4/3$ for larger-than-magic angle tBLG, by constructing the WOs of each valley using the projection method²³ and by including direct density–density interaction V 's and the direct exchange interaction J 's up to third nearest neighbour (Fig. 2b and Supplementary Fig. S5). Notably, substantial differences exist between the WOs constructed from the two valleys on the same site (Fig. 2a). Thus, the SU(4) spin-valley symmetry, which is conventionally assumed in calculations, is broken. Instead, the resulting Hamiltonian has a $\text{SU}(2) \times \text{SU}(2) \times \text{U}(1)$, symmetry, which accounts for the separate spin-rotation symmetry for each valley and the valley polarization conservation.

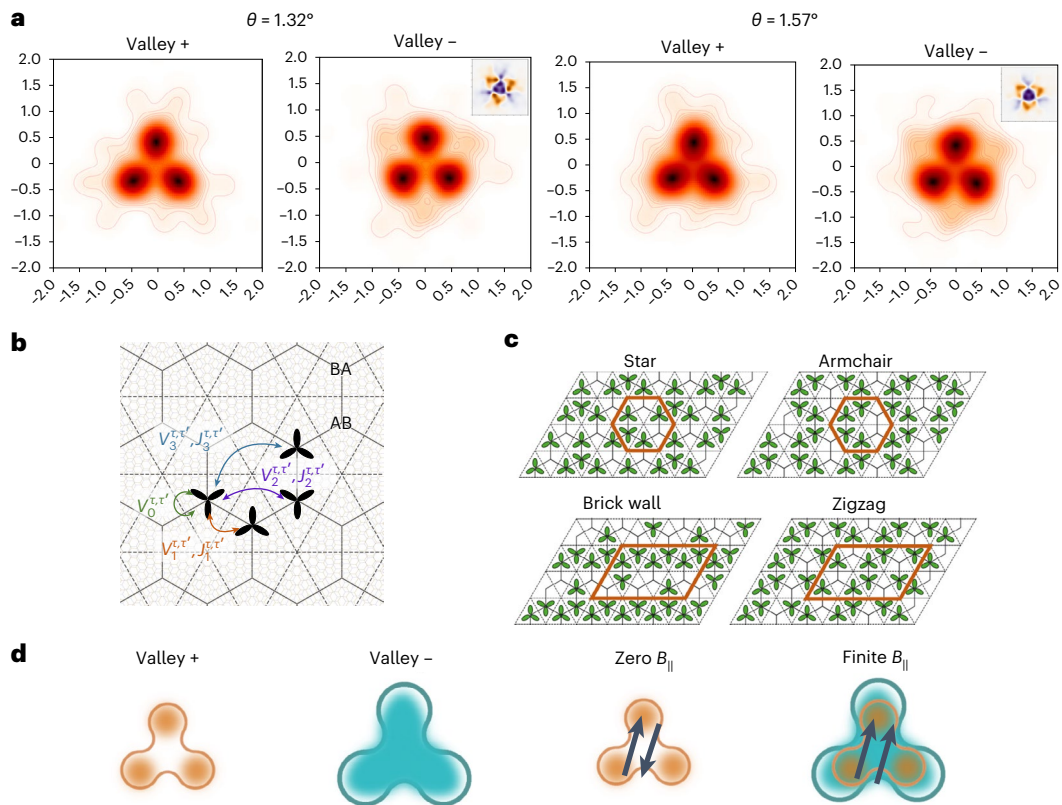


Fig. 2 | Real-space model. **a**, WOs at BA sites for two different twist angles. Insets: The difference between the WOs of the two valleys. **b**, Model with direct density–density interaction (V terms) and direct exchange (J terms) up to third nearest neighbour. AB and BA refer to the local stacking order, and τ and τ' are spin/valley indices. **c**, Schematic of states close in energy at $\tilde{n} = -8/3$. The charge

configurations at $\tilde{n} = -4/3$ can be obtained from turning unoccupied sites in the configuration into doubly occupied sites (Supplementary Information). **d**, Schematic of the WOs (left) and the competition (right) between the spin-singlet, valley-polarized state at zero field and the spin-polarized, valley-anti-aligned state at finite field for the sites with double occupation at $\tilde{n} = \pm 4/3$.

Like the case at $\tilde{n} = -4 + 1/3$ discussed in refs. 8,19, exchange interactions promote ferromagnetic spin and valley alignment, and the distinct valley WOs imply that Coulomb interactions favour valley-locking at AB/BA sublattice sites. On the other hand, charge sharing at higher fillings at $\tilde{n} = \pm 8/3$ or $\pm 4/3$ (counting from the empty band at $\tilde{n} = -4$) forces WO touching, resulting in close competition between a rich set of possibilities¹⁹, which is the signature of a geometrically frustrated system. The balance between different interaction strengths determines the ground state.

At $\tilde{n} = \pm 8/3$, four electrons or holes are shared among three moiré cells. Thus, each moiré site is either empty or singly occupied. We find four competing charge configurations (Fig. 2c): two with a threefold unit cell enlargement (the star and armchair phases) and two with a sixfold enlargement (brick-wall and zigzag phases). At $\theta = 1.32^\circ$, the brick-wall phase is narrowly favoured over all the other phases, although the enlarged unit cell is not expected to be detected in transport due to the residual local degeneracy¹⁹ (Supplementary Information Discussion E.3). Moreover, the direct exchange interactions favour aligning the spin and valley between neighbouring sites. Thus, we anticipate the $\tilde{n} = \pm 8/3$ ground state to be a spin and valley-polarized ferromagnetic insulator. Thermally excited conduction in this state requires sites to be doubly occupied. Thus, the thermal activation gap is of the order of the energy cost of double occupation, which we estimate is approximately 20 meV (Supplementary Information), consistent with the experimentally observed gap size.

For $\tilde{n} = \pm 4/3$, eight electrons (holes) must be accommodated among three moiré cells, so at least two sites must be doubly occupied, leading to additional geometric frustration and richness. Direct Coulomb interactions favour the formation of a valley-polarized state in

doubly occupied sites, although Pauli exclusion requires such doubly occupied sites to be in a spin-singlet state (Fig. 2d) at zero field. At low temperatures, the conductance comes from the electrons in the doubly occupied sites flowing on top of the singly occupied background. The thermal activation gap is, thus, of the order of further neighbour interactions instead of on-site repulsion, leading to a smaller gap than at $\tilde{n} = \pm 8/3$, in agreement with observations. Moreover, our model suggests that the $\tilde{n} = \pm 8/3$ and $\tilde{n} = \pm 4/3$ states should respond differently to in-plane magnetic fields: a stabilized ferromagnetic phase and a singlet–triplet transition are expected, respectively.

We now investigate these $1/3$ -filling states in a magnetic field to probe the Landau-level structure and spin states. Figure 3a,b displays the conductance G versus charge density and perpendicular magnetic field B and the corresponding Wannier diagram identifying features in G with the numbers indicating the Chern number t in equation (1). At the CNP and $B = 0$, symmetric Landau fans radiate into both electron and hole regimes, like those observed in MA-tBLG devices^{1,24–27}. The conductance of all fractional-filling-factor states decreases with B , as shown in Fig. 3c,d. (An exception is the state at $\tilde{n} = +4/3$, where $G(B)$ is almost constant. This asymmetry compared to $\tilde{n} = -4/3$ may arise from electron–hole asymmetry in the band structure or from different effects of nearby Landau levels emanating from $\tilde{n} = 0$). Although no Landau fan is observed at $\tilde{n} = \pm 8/3$, Landau fans emerge at $\tilde{n} = -4/3$ and $2/3$, appearing to the left (right) of the hole-doped (electron-doped) regime, respectively, with a twofold degeneracy.

These asymmetric or one-sided Landau fans are reminiscent of those at $\tilde{n} = \pm 2$ and ± 3 in MA-tBLG devices, in which a phase transition and a reconstruction of the Fermi surface occurs, yielding a reset of the band structure to the Dirac point^{24,28,29}. Here we see a similar reset,

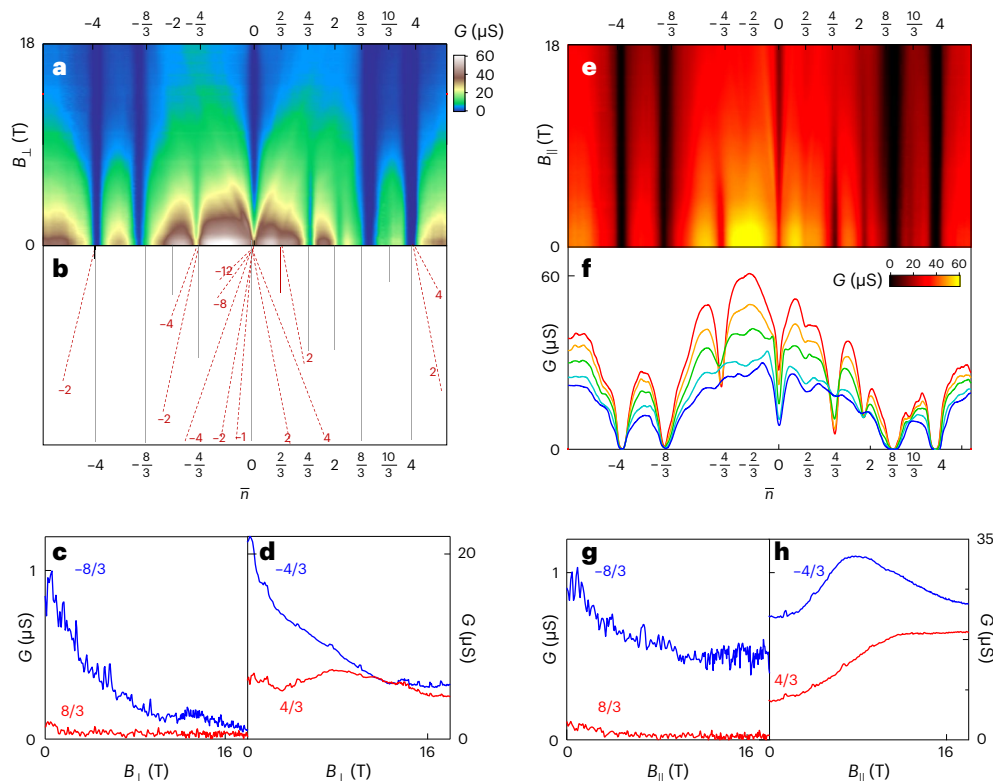


Fig. 3 | Magnetotransport of device D1 at $T = 300$ mK. a, b, Two-terminal $G(\bar{n}, B_{\perp})$ in microsiemens (a) and Wannier diagram identifying features in (b). Numbers indicate corresponding t quantum numbers. **c, d**, $G(B_{\perp})$ at $\bar{n} = \pm 8/3$ (c) and $\pm 4/3$ (d). **e, f**, $G(\bar{n}, B_{\parallel})$ in microsiemens (e) and line traces at $B_{\parallel} = 0, 3, 6, 12$ and 18 T (top to bottom) (f). **g, h**, $G(B_{\parallel})$ at $\bar{n} = \pm 8/3$ (g) and $\pm 4/3$ (h).

and the degeneracy of the two indicates isospin polarization. On the other hand, since the reset occurs at fractional-filling factors in this large-angle device, rather than for the integer \bar{n} values in magic-angle devices, both the underlying phase transition and the reconstructed ground state are probably very different.

The presence or absence of a Landau fan at different fractional fillings indicate that they host different electronic ground states. To further explore their nature and to study magnetic ordering at $\bar{n} = \pm 8/3$, we apply an in-plane magnetic field B_{\parallel} , which induces Zeeman splitting. Figure 3e, f plots $G(\bar{n}, B_{\parallel})$ and line traces at $B_{\parallel} = 0, 3, 6, 12$ and 18 T, respectively. The conductance of the states at $\bar{n} = \pm 8/3$ decreases with increasing in-plane field. This suggests an increasing gap, such as that of a spin-polarized state (Fig. 3g). This observation provides evidence for the predicted brick-wall state's valley-polarized spin-ferromagnetic fractional insulating ground state. Here every site is covered by the extended WOs with spin and valley polarization, so spin flips are needed for conduction. Hence, increasing B_{\parallel} raises the energy cost of spin flips and leads to an enhanced activation gap or lower conductivity, as observed.

The situation at $\bar{n} = \pm 4/3$ differs, however. The conductance of the state at $\bar{n} = 4/3$ increases with increasing B_{\parallel} , suggesting the closing of an energy gap, such as that of an antiferromagnetic state (Fig. 3h). Interestingly, the state at $\bar{n} = -4/3$ exhibits nonmonotonic dependence on B_{\parallel} , thus hinting at the closing and opening of a gap at $B_{\parallel} \approx 8$ T. Taken together, these different behaviours of states at $\bar{n} = \pm 4/3$ suggest the presence of states with several competing magnetic orders arising from orbital and spin geometric frustration, which are consistent with the many competing ground states of the parent integer states at $\bar{n} = \pm 1$ (refs. 30–35). The observed nonmonotonic G versus B_{\parallel} dependence thus arises from competition between the spin-singlet and spin-polarized states at the doubly occupied sites of $\bar{n} = \pm 4/3$. B_{\parallel} introduces a Zeeman term that favours a spin-polarized, valley-anti-aligned

state (Fig. 2d), but a finite B_{\parallel} is required for the Zeeman energy to overcome the Coulomb-driven valley polarization. Hence, increasing B_{\parallel} initially reduces the transport gap and increases the conductivity, until the spin-triplet phase becomes the ground state, whence the increase in B_{\parallel} increases the transport gap, resulting in decreasing G . The observed nonmonotonic behaviour for the $4/3$ -filling states under an in-plane magnetic field supports this expectation of frustration-induced competition between spin-singlet and spin-polarized states at the doubly occupied sites of $4/3$ filling. The maximum G at $B_{\parallel} \approx 10$ T suggests an energy scale of approximately 1 meV for the valley polarization energy scale.

Returning to the competing states in Fig. 2b, a different ground state can be realized by changing the balance between the various extended interaction terms. This can be achieved by tuning the twist angle. A large θ results not only in a smaller moiré unit cell but also modifications in the competition between the second and third nearest neighbour interactions. At a larger twist angle, our model predicts that the armchair phase becomes narrowly favoured over the brick-wall phase due to an increase of the second nearest neighbour interaction with respect to the third nearest neighbour ones, resulting in a tripling of the unit cell relative to the moiré unit cell (Supplementary Table 5).

These predictions, in particular the unit cell tripling, are borne out experimentally in a second device D2 that has a larger twist angle $\theta = 1.59 \pm 0.02^{\circ}$. Like D1, it displays prominent four-probe longitudinal-resistance features R_{xx} at $\bar{n} = \pm 8/3$ and $\pm 4/3$ (their thermal activation behaviour is not well resolved due to the reduced correlation among charge carriers), while showing strongly suppressed peaks at $\bar{n} = \pm 2$, as shown in Fig. 4a. At finite magnetic field, several Landau-fan features at $1/3$ -fractional filling appear. Here the Landau fans emanate from their zero-field peaks in both doping directions (Fig. 4b). The resolved Landau levels with corresponding quantum t numbers are sketched in Fig. 4c. The Landau fan emanating from the CNP is electron–hole

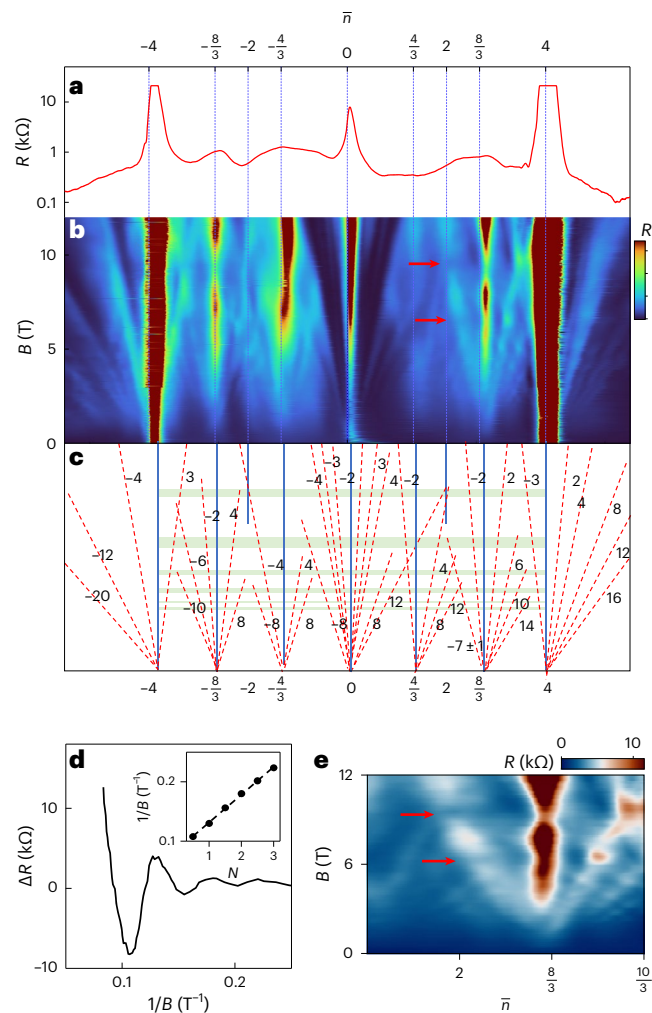


Fig. 4 | Magnetotransport of device D2 at $T = 1.5$ K. **a, b**, Four-terminal longitudinal resistance $R(\bar{\nu})$ at $B = 0$ (**a**) and $R(\bar{\nu}, B)$ in kilohms (**b**). **c**, Wannier diagram identifying features in **b**. Numbers indicate corresponding t quantum numbers. Horizontal green bands mark Brown–Zak oscillations. **d**, Line trace taken at filling $8/3$ versus $1/B$ (a polynomial background fit was subtracted). Inset: $1/B$ values of N th maxima (N th/2 minima) extracted from the main panel. The slope of the fitted line enables a determination of the period in $1/B$. **e**, Zoom-in plot of region in **b** near $\bar{\nu} = 8/3$, showing the density-independent resistance minima in Brown–Zak bands.

symmetric, where the degeneracy of the lowest Landau level is fully resolved. The rest of the Landau fan is fourfold degenerate, with spectral gaps observed at $t = 4N$, where N is an integer. Similar Landau fans with $t = 4N$ spectral gaps are observed to emanate from $\bar{\nu} = -4/3$, where the degeneracy is doubled compared to D1 and is probably due to the broadening of the Hofstadter bands in D2 since the kinetic energy is larger for a larger twist angle. Interestingly, for the Landau fan centred at $\bar{\nu} = \pm 8/3$, spectral gaps are electron–hole asymmetric: states at $t = 2, 6, 10, \dots$ are resolved in the electron and hole side for $\bar{\nu} = 8/3$ and $-8/3$, respectively, whereas those at $t = 4$ and 8 are resolved on the other side. This asymmetry of the Landau-level gaps indicates that when tuning across $\bar{\nu} = \pm 8/3$, the Berry phase experienced by the charge carriers undergoing cyclotron orbits changes abruptly from 0 to π (modulo 2π), which in turn suggests a reset of the effective band structure. Note also that, like D1, the trajectory of these gapped states is vertical, which implies zero Chern number.

A detailed examination of the Fig. 4b data reveals a tripled unit cell for the states at $\bar{\nu} = \pm 8/3$. Red arrows in Fig. 4b and horizontal green bands in Fig. 4c mark features extending across the data independent

of density. These so-called Brown–Zak oscillations³⁶ arise in Hofstadter systems whenever the magnetic field is tuned such that $b = p/q$ in equation (1) for mutually prime integers p and q . In this case, the translational symmetry is restored and the effective quasiparticles move in a zero effective magnetic field. Plotting R_{xx} versus $1/B$ shows a periodic oscillation (Fig. 4d). The longest period and largest amplitude oscillations are expected to occur when $p = 1$ (ref. 36). The inset of Fig. 4d shows the N th minimum (maximum) plotted versus their number. The data closely follow a straight line from which the oscillation period $1/B_F$ is extracted. Using $B_F A_e = h/e$ at the minima, where A_e is the effective unit cell area, we find a unit cell area of $A_e = (1.94 \pm 0.03) \times 10^{-16} \text{ m}^2$. Based on the twist angle of 1.57° , we find the moiré unit cell area is $A = (6.8 \pm 0.27) \times 10^{-17} \text{ m}^2$. The ratio $A_e/A \approx 2.85 \pm 0.1$ is consistent with a 3:1 reconstruction of the effective unit cell area. This reconstruction extends over a finite range in density. The observed tripled unit cell and the observed zero Chern number provide strong evidence for either armchair or star phases. The two phases are close in energy, with armchair being slightly favoured, reflecting orbital geometric frustration. In addition, the fourfold degeneracy of the Landau levels at the CNP indicates C_3 breaking, compatible with the armchair phase. Finally, note that the evidence for the threefold unit cell expansion is not as clear when crossing to a higher density than $8/3$ filling (Fig. 4e). This may reflect a change in the unit cell that accompanies the reset behaviour and Berry phase change, as discussed above.

Online content

Any methods, additional references, Nature Portfolio reporting summaries, source data, extended data, supplementary information, acknowledgements, peer review information; details of author contributions and competing interests; and statements of data and code availability are available at <https://doi.org/10.1038/s41567-024-02546-5>.

References

- Cao, Y. et al. Correlated insulator behaviour at half-filling in magic-angle graphene superlattices. *Nature* **556**, 80–84 (2018).
- Padhi, B., Setty, C. & Phillips, P. W. Doped twisted bilayer graphene near magic angles: proximity to Wigner crystallization, not Mott insulation. *Nano Lett.* **18**, 6175–6180 (2018).
- Padhi, B. & Phillips, P. W. Pressure-induced metal–insulator transition in twisted bilayer graphene. *Phys. Rev. B* **99**, 205141 (2019).
- Regan, E. C. et al. Mott and generalized Wigner crystal states in WSe_2/WS_2 moiré superlattices. *Nature* **579**, 359–363 (2020).
- Xu, Y. et al. Correlated insulating states at fractional fillings of moiré superlattices. *Nature* **587**, 214–218 (2020).
- Li, H. et al. Imaging two-dimensional generalized Wigner crystals. *Nature* **597**, 650–654 (2021).
- Padhi, B., Chitra, R. & Phillips, P. W. Generalized Wigner crystallization in moiré materials. *Phys. Rev. B* **103**, 125146 (2021).
- Zhang, K., Zhang, Y., Fu, L. & Kim, E.-A. Fractional correlated insulating states at one-third filled magic-angle twisted bilayer graphene. *Commun. Phys.* **5**, 250 (2022).
- Zhou, Y. et al. Bilayer Wigner crystals in a transition metal dichalcogenide heterostructure. *Nature* **595**, 48–52 (2021).
- Lau, C. N., Bockrath, M. W., Mak, K. F. & Zhang, F. Reproducibility in the fabrication and physics of moiré materials. *Nature* **602**, 41–50 (2022).
- Streda, P. Quantised Hall effect in a two-dimensional periodic potential. *J. Phys. C* **15**, L1299 (1982).
- MacDonald, A. Landau-level subband structure of electrons on a square lattice. *Phys. Rev. B* **28**, 6713 (1983).
- Spanton, E. M. et al. Observation of fractional Chern insulators in a van der Waals heterostructure. *Science* **360**, 62–66 (2018).
- Cheng, B. et al. Fractional and symmetry-broken Chern insulators in tunable moiré superlattices. *Nano Lett.* **19**, 4321–4326 (2019).

15. Xie, Y. et al. Fractional Chern insulators in magic-angle twisted bilayer graphene. *Nature* **600**, 439–443 (2021).
16. Rickhaus, P. et al. Correlated electron-hole state in twisted double-bilayer graphene. *Science* **373**, 1257–1260 (2021).
17. Li, Q. et al. Tunable quantum criticalities in an isospin extended Hubbard model simulator. *Nature* **609**, 479–484 (2022).
18. Shen, C. et al. Dirac spectroscopy of strongly correlated phases in twisted trilayer graphene. *Nat. Mater.* **22**, 316–321 (2023).
19. Mao, D., Zhang, K. & Kim, E.-A. Fractionalization in fractional correlated insulating states at $n \pm 1/3$ filled twisted bilayer graphene. *Phys. Rev. Lett.* **131**, 106801 (2023).
20. Kang, J. & Vafek, O. Symmetry, maximally localized Wannier states, and a low-energy model for twisted bilayer graphene narrow bands. *Phys. Rev. X* **8**, 031088 (2018).
21. Koshino, M. et al. Maximally localized Wannier orbitals and the extended Hubbard model for twisted bilayer graphene. *Phys. Rev. X* **8**, 031087 (2018).
22. Po, H. C., Zou, L., Vishwanath, A. & Senthil, T. Origin of Mott insulating behavior and superconductivity in twisted bilayer graphene. *Phys. Rev.* **8**, 031089 (2018).
23. Marzari, N., Mostofi, A. A., Yates, J. R., Souza, I. & Vanderbilt, D. Maximally localized Wannier functions: theory and applications. *Rev. Mod. Phys.* **84**, 1419 (2012).
24. Lu, X. et al. Superconductors, orbital magnets, and correlated states in magic-angle bilayer graphene. *Nature* **574**, 653–657 (2019).
25. Yankowitz, M. et al. Tuning superconductivity in twisted bilayer graphene. *Science* **363**, 1059–1064 (2019).
26. Tian, H. et al. Evidence for Dirac flat band superconductivity enabled by quantum geometry. *Nature* **614**, 440–444 (2023).
27. Codecido, E. et al. Correlated insulating and superconducting states in twisted bilayer graphene below the magic angle. *Sci. Adv.* **5**, eaaw9770 (2019).
28. Balents, L., Dean, C. R., Efetov, D. K. & Young, A. F. Superconductivity and strong correlations in moiré flat bands. *Nat. Phys.* **16**, 725–733 (2020).
29. Zondiner, U. et al. Cascade of phase transitions and Dirac revivals in magic-angle graphene. *Nature* **582**, 203–208 (2020).
30. Saito, Y. et al. Hofstadter subband ferromagnetism and symmetry-broken Chern insulators in twisted bilayer graphene. *Nat. Phys.* **17**, 478–481 (2021).
31. Stepanov, P. et al. Competing zero-field Chern insulators in superconducting twisted bilayer graphene. *Phys. Rev. Lett.* **127**, 197701 (2021).
32. Nuckolls, K. P. et al. Strongly correlated Chern insulators in magic-angle twisted bilayer graphene. *Nature* **588**, 610–615 (2020).
33. Choi, Y. et al. Correlation-driven topological phases in magic-angle twisted bilayer graphene. *Nature* **589**, 536–541 (2021).
34. Wu, S., Zhang, Z., Watanabe, K., Taniguchi, T. & Andrei, E. Y. Chern insulators, van Hove singularities and topological flat bands in magic-angle twisted bilayer graphene. *Nat. Mater.* **20**, 488–494 (2021).
35. Das, I. et al. Symmetry-broken Chern insulators and Rashba-like Landau-level crossings in magic-angle bilayer graphene. *Nat. Phys.* **17**, 710–714 (2021).
36. Krishna Kumar, R. et al. High-temperature quantum oscillations caused by recurring Bloch states in graphene superlattices. *Science* **357**, 181–184 (2017).

Publisher's note Springer Nature remains neutral with regard to jurisdictional claims in published maps and institutional affiliations.

Springer Nature or its licensor (e.g. a society or other partner) holds exclusive rights to this article under a publishing agreement with the author(s) or other rightsholder(s); author self-archiving of the accepted manuscript version of this article is solely governed by the terms of such publishing agreement and applicable law.

© The Author(s), under exclusive licence to Springer Nature Limited 2024

Data availability

Source data are provided with this paper. The data that support the findings of this study are available from the corresponding authors on reasonable request.

Code availability

The code that supports the findings of this study is available from the corresponding authors upon reasonable request.

Acknowledgements

We thank F. Zhang for helpful discussions. The experiments were supported by the Basic Energy Sciences division of the Department of Energy (Grant No. DE-SC0020187). Devices were fabricated using a nanofabrication facility supported by the Materials Research Science and Engineering Center of the National Science Foundation (NSF; Grant No. DMR-2011876). D.M. and E.-A.K. are supported by the Gordon and Betty Moore Foundation's EPIQS Initiative (Grant No. GBMF10436). K.Z. is supported by the NSF (Grant No. EAGER OSP-136036) and the Natural Sciences and Engineering Research Council of Canada (Grant No. PGS-D-557580-2021). E.-A.K. acknowledges support from the Ewha Frontier 10-10 Research Grant and the Simons Fellowship in Theoretical Physics (Award 920665). A portion of this work was performed at the National High Magnetic Field Laboratory, which is supported by the NSF (Grant No. NSF/DMR-1644779) and the State of Florida. K.W. and T.T. acknowledge support from the JSPS KAKENHI

(Grant Nos. 21H05233 and 23H02052) and World Premier International Research Center Initiative, MEXT, Japan.

Author contributions

C.N.L. and M.B. conceived the project. H.T. and E.C. fabricated devices with assistance from S.C. H.T., E.C. and D.S. performed the measurements. K.W. and T.T. provided the hBN crystals. D.M. and K.Z. performed the theoretical calculations under the supervision of E.-A.K. C.N.L. and M.B. analysed the data. C.N.L., M.B., E.-A.K. and D.M. interpreted the data and wrote the paper. All authors read and commented on the paper.

Competing interests

The authors declare no competing interests.

Additional information

Supplementary information The online version contains supplementary material available at <https://doi.org/10.1038/s41567-024-02546-5>.

Correspondence and requests for materials should be addressed to Eun-Ah Kim, Marc Bockrath or Chun Ning Lau.

Peer review information *Nature Physics* thanks the anonymous reviewers for their contribution to the peer review of this work.

Reprints and permissions information is available at www.nature.com/reprints.